Journal of Hazardous Materials 217–218 (2012) 238–245

Contents lists available at SciVerse ScienceDirect

Journal of Hazardous Materials

journal homepage: www.elsevier.com/locate/jhazmat

Arsenate immobilization associated with microbial oxidation of ferrous ion in complex acid sulfate water

Yingqun Ma[a], Chuxia Lin[b,*]

[a] Centre for Ecological and Environmental Technologies, South China Agricultural University, Guangzhou 510642, China
[b] Australian Centre for Sustainable Catchments, University of Southern Queensland, Toowoomba QLD 4350, Australia

ARTICLE INFO

Article history:
Received 12 December 2011
Received in revised form 24 February 2012
Accepted 7 March 2012
Available online 15 March 2012

Keywords:
Arsenic
Acid sulfate water
Ochreous precipitate
Co-precipitation
Adsorption

ABSTRACT

Chemical, XRD, SEM, RS, FTIR and XPS techniques were used to investigate arsenate immobilization associated with microbial Fe^{2+} oxidation in a complex acid sulfate water system consisting of a modified 9 K solution (pH 2.0) plus As, Cu, Cd, Pb, Zn and Mn. At a 1:12.5:70 molar ratio of As:Fe:S, schweretmannite formation was impeded. This was in contrast with the predominant presence of schwertmannite when the heavy metals were absent, suggesting that a schwertmannite binding model is not valid for explaining arsenate immobilization in the complex system. In this study, arsenate was initially immobilized through co-precipitation with non-Fe metals and phosphate. Subsequently when sufficient Fe^{3+} was produced from Fe^{2+} oxidation, formation of a mixed iron, arsenate and phosphate phase predominated. The last stage involved surface complexation of arsenate species. Pb appeared to play an insignificant role in arsenate immobilization due to its strong affinity for sulfate to form anglesite. Phosphate strongly competed with arsenate for the available binding sites. However, As exhibited an increased capacity to compete with P and S for available binding sites from the co-precipitation to surface complexation stage. Adsorbed As tended to be in $HAsO_4^{2-}$ form. The scavenged arsenate species was relatively stable after 2464-h aging.

1. Introduction

Arsenic is frequently associated with acid sulfate waters originating from mined areas where sulfidic rocks occur [1,2]. Ferrous sulfate ($FeSO_4$) is the major constitute of acidic mine water, and the mine water-borne Fe^{2+} tends to oxidize to Fe^{3+} and subsequently hydrolyse, resulting in the generation of H^+ and formation of orchreous precipitates. It has been demonstrated that in some acid sulfate water systems, poorly crystalline schwertmannite ($Fe_8O_8(OH)_6SO_4$) is initially formed in a pH range of 2.8–4.5 [3,4]. Schwertmannite is then gradually transformed into more stable mineral phases such as goethite (FeOOH) or/and jarosite ($KFe_3(OH)_6(SO_4)_2$) following aging [5–10]. Due to their large specific surface area, ochreous precipitates (especially schwertmannite) possess a strong capacity to scavenge aqueous arsenate under acidic conditions [11–13]. This geochemical process is viewed to be responsible for the natural attenuation of mine water-borne arsenates [14–16]. Sorption of arsenate to pre-prepared schwertmannite has been investigated in the laboratory by some workers [17,18]. However, such processes are not relevant to natural acid mine drainage scenarios that involve spontaneous formation of solid phases from mixed Fe, S and As systems where co-precipitation is likely to occur [11].

In abiotic co-precipitation experiments involving arsenate and other oxyanions (chromate and phosphate), Regenspurg et al. [19] found that the characteristic XRD peaks of schwertmannite disappeared when sufficient amounts of arsenate were present in the systems, suggesting the formation of other mineral phases rather than schwertmannite. The similar phenomena were also observed in the Fe–S–P system in their experiments. It is therefore likely that in more complex acid sulfate water systems, the immobilization of arsenate cannot be simply explained by a schwertmannite co-precipitation and adsorption model. This could be particularly true when the acid sulfate water contains sufficiently high concentration of heavy metals such as Cu, Cd, Pb, Zn and Mn, which can react with arsenate to form sparsely soluble or "insoluble" compounds. Moreover, the system can be further complicated due to the presence of other oxyanions such as phosphate, which may compete with arsenate for available binding sites. Also ferrous ion oxidation in actual mine water is predominantly mediated by iron-oxidizing bacteria since abiotic oxidation of ferrous ion using molecular oxygen as an oxidant is very slow under acidic conditions [20,21]. It has been known that iron-oxidizing bacteria are not only responsible for the oxidation of ferrous ion but also have a role to play in the formation of iron precipitates [22,23]. Therefore, laboratory

* Corresponding author. Tel.: +61 7 46312429; fax: +61 7 46315581.
E-mail addresses: Chuxia.Lin@usq.edu.au, cxlin@scau.edu.cn (C. Lin).

0304-3894/$ – see front matter © 2012 Elsevier B.V. All rights reserved.
doi:10.1016/j.jhazmat.2012.03.021

experiments that use abiotic methods for Fe–S–As co-precipitation may not well simulate the process that takes place in the field conditions.

To the best of our knowledge, there has not been any detailed investigation into the microbially mediated oxidation of aqueous Fe^{2+} and the resulting arsenate immobilization by precipitate formation in acid sulfate water systems with complex chemical composition. In this study, a microcosm experiment was conducted to take into account a microbial factor and a multi-element scenario. The objectives of this study were to (a) understand the chemical behaviour of arsenic and other elements during the microbially mediated oxidation of aqueous Fe^{2+} in the complex acid sulfate water system; (b) characterize the precipitates formed during the period of incubation experiment; and (c) to depict the reaction mechanisms that were responsible for the observed arsenate immobilization in the investigated aqueous system.

2. Materials and methods

2.1. Bacteria, culture conditions and inoculum preparation

A strain of *Acidithiobacillus ferrooxidans* was purchased from the Marine Culture Collection of China (MCCC). The bacterial culture was maintained at 4 °C in a 9 K nutrient medium containing 3.0 g of $(NH_4)_2SO_4$, 0.01 g of $Ca(NO_3)_2$, 0.5 g of $MgSO_4{\cdot}7H_2O$, 0.5 g of K_2HPO_4, 0.1 g of KCl and 44.3 g of $FeSO_4{\cdot}7H_2O$ in 1 L of distilled water with the pH adjusted to 1.6 with a H_2SO_4 solution.

The inoculum was prepared prior to the incubation experiment. An adequate amount of the bacteria required for the experiment was produced by facilitating bacterial growth in a sterile 9 K medium at 30 °C, coupled with shaking (130 rpm) on a rotary shaker for 5–6 days. The cells in the enriched suspension were firstly separated from the iron precipitates (formed during the incubation) by centrifugation at 3000 rpm for 3 min to allow the settlement of the solid iron compounds. The cells remained in the suspension were then harvested by centrifugation at 5000 rpm for 10 min to allow the settlement of the cells. After washing twice with sterile distilled water (adjusted to pH 2.0 by a H_2SO_4 solution), the inoculum was formed by adding an appropriate amount of the same acidified distilled water into the centrifuge tube containing the cleaned cells. The cell concentration in the inoculum was determined by direct cell counting prior to addition into the experimental reactor. For this experiment, the cell concentration of the inoculum was 4.5×10^8 cells mL^{-1}.

2.2. Experimental design

Twenty litres of the modified 9 K medium was used as the basal solution for the incubation experiment. The solution contained 10 mmol L^{-1} of $FeSO_4{\cdot}7H_2O$, 0.8 mmol L^{-1} of Na_2HAsO_4, 17.9 mmol L^{-1} of $(NH_4)_2SO_4$, 0.09 mmol L^{-1} of $Ca(NO_3)_2$, 2.35 mmol L^{-1} of $MgSO_4{\cdot}7H_2O$, 2.74 mmol L^{-1} of K_2HPO_4, 1.35 mmol L^{-1} of KCl, 1.07 mmol L^{-1} of $CuSO_4{\cdot}5H_2O$, 0.3 mmol L^{-1} of $Pb(NO_3)_2$, 0.91 mmol L^{-1} of $ZnSO_4{\cdot}7H_2O$, 0.12 mmol L^{-1} of $CdSO_4$ and 1.2 mmol L^{-1} of $MnSO_4{\cdot}H_2O$. The pH of the solution was adjusted to 2 by a H_2SO_4 solution and then 20 mL of the inoculum was added into the solution to allow a theoretical cell concentration of 4.5×10^5 mL^{-1} at the beginning of the incubation experiment.

Various water chemical parameters were monitored during the Phase I of the incubation experiment (996 h). The first and second water samples (in triplicate) were collected 30 min. and 2 h after the addition of the inoculum, respectively. Subsequent water sample collection was performed at a time interval ranging from 2 to 7 days. Immediately after each sample collection, the water samples were passed through a 0.2 μm membrane filter and then stored in a refrigerator prior to analysis.

At the 996th h of the experiment, approximately half of the precipitates were harvested. This was done by thoroughly mixing the mud slurry after removing the supernatant. The mixed slurry was then divided into two equal parts; one part was centrifuged to obtain the sediments for various chemical and mineralogical analyses. Another part returned to the solution to allow continuation of the incubation experiment for another 2464 h (Phase II). At the end of the experiment, the sediment was harvested for various chemical and mineralogical analyses.

2.3. Water sample analysis

In situ measurement of pH in the solution was made by a calibrated pH meter (Model pHS-3C, manufactured by the Shanghai Scientific Instrument Limited.). Dissolved oxygen (DO) was measured by a JPB-607 DO meter (manufactured by the Shanghai Scientific Instrument Limited.). Ferrous ion (Fe^{2+}) was measured by the potassium dichromate titration method [24]. Various elements in the solution were determined by inductively coupled plasma–atomic emission spectroscopy (ICP-AES) using an Agilent 735 Series ICP-OES Spectrometer.

2.4. Precipitate sample analysis

After air-drying, the precipitate sample was ground to fineness. Total element composition was determined by ICP-AES after digestion of a sample with a mixed $HCl/HNO_3/HClO_4$/HF solution.

Mineralogical characterization was performed using Raman spectroscopy (RS), Fourier transform infrared spectroscopy (FTIR) and X-ray diffraction (XRD). RS was analyzed using a HORIBA Jobin Yvon Lab Ram Aramis spectrometer. FTIR analysis was performed using a Bruker VEVTOR 33 FTIR spectrometer. XRD analysis was conducted using a Bruker D8 180 ADVANCE X-ray diffractometer. The Materials Data Inc. software Jade 181 5.0 was used for phase identification.

A FEI-XL30 environmental scanning electron microscope coupled with energy dispersive X-ray spectrometer (ESEM/EDS) was used for surface imaging. The X-ray photoelectron spectroscopy (XPS) was also employed to determine the chemical composition and chemical state of the precipitates (to a depth of approximately 3 nm). XPS analyses were performed with a Kratos Axis $Ultra^{DLD}$ spectrometer using a monochromatic Al Kα X-rays source. Broad scan was conducted using 160 eV pass energy, while narrow high-resolution spectra of all major lines were obtained using a resolution function with a width of 0.1 eV for a pass energy setting of 40 eV. The charge effect was corrected using C 1s from contamination at 284.6 eV. Spectra were analyzed using the CasaXPS software (Version 2.2.19).

2.5. Quality assurance and quality control

The analyses of various elements in all the water and precipitate samples were conducted in the ALS Chemex Guangzhou Laboratory, which has a strict QA/QC procedure in place for all sample analysis, including the use of certified reference material (CRM05-OREAS 45P), duplicates and blanks. Repeatability analysis of the replicated data ($n = 3$) shows that the mean RSD is less than 5% for all the tested water chemical parameters.

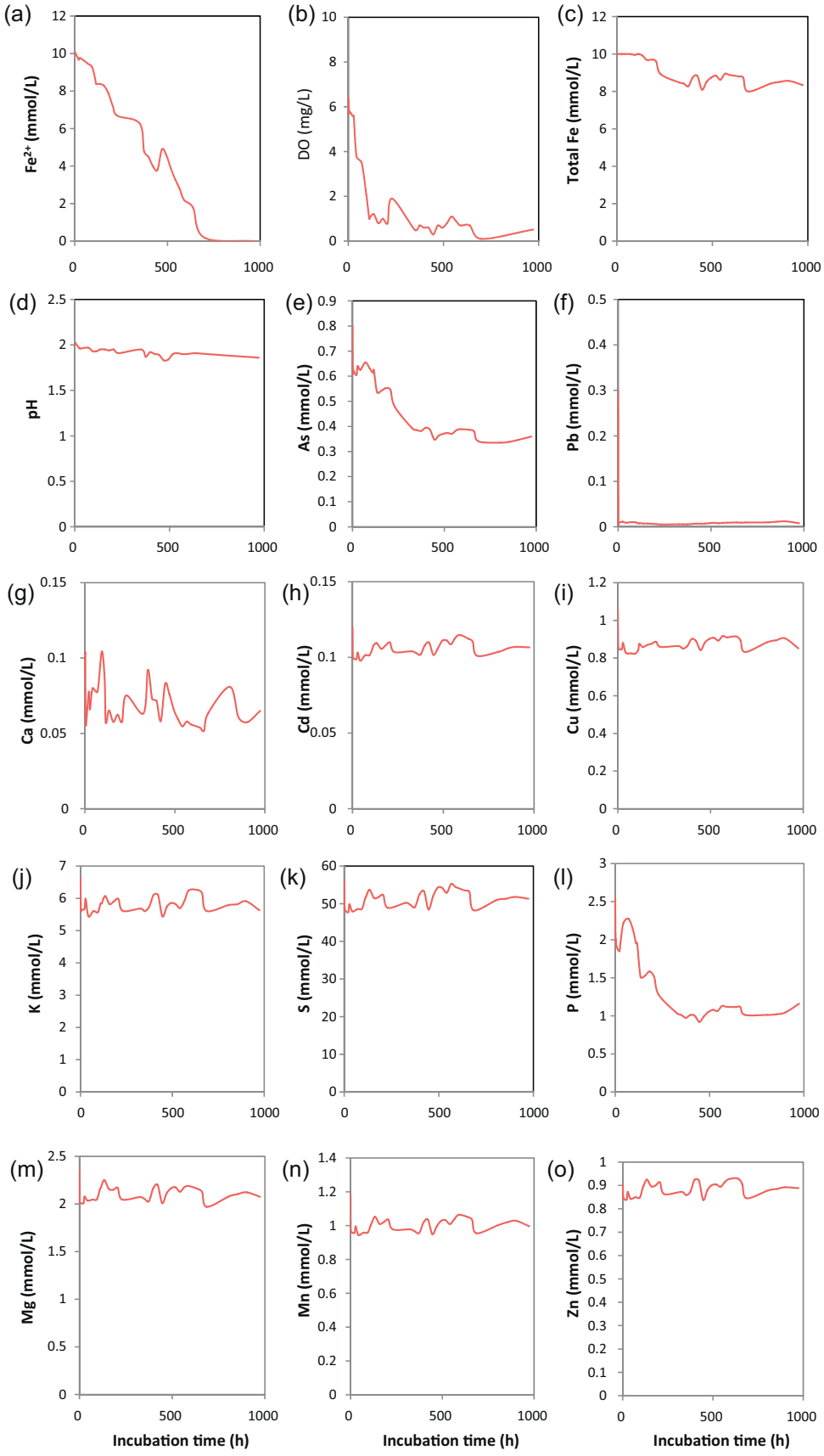

Fig. 1. Changes in various water chemical parameters during Phase I (996 h) of the incubation experiment.

3. Results and discussion

3.1. Water-borne element evolution in Phase I of the incubation experiment

The dynamics of various water chemical parameters during Phase I of the incubation experiment (996 h) are shown in Fig. 1. Ferrous ion (Fe^{2+}) concentration decreased progressively over time and almost completely disappeared after approximately 686 h of the microbially mediated oxidation (Fig. 1a). This was accompanied by a sharp decrease in dissolved oxygen (DO) from the initial 6.4 mg L^{-1} to 1.0 mg L^{-1} at the 110th h of the experiment, followed by a gentler decrease, with marked fluctuation, to nearly zero at the 686th h before it re-increased to 0.5 mg L^{-1} at the 996th h (Fig. 1b). However, total Fe concentration remained little change during the initial 116 h of the experiment, indicating that precipitation of the newly formed ferric ion was insignificant during this period. Relatively marked drop in total Fe took place during the period from the 116th to the 374th h and then fluctuated between 8.0 and 8.9 mmol L^{-1}. Overall, there was still over 83% of the originally added Fe that remained in the solution at the end of Phase I of the experiment (Fig. 1c). The maintenance of high total Fe concentration in the solution was attributable to the generally low pH, which sustained high Fe^{3+} concentration in the solution [25]. There was a trend that the solution pH decreased over time (Fig. 1d), reflecting the production of H^+ resulting from the precipitation of ferric ion [26] that was progressively converted from ferrous ion.

It is interesting to note that there was a sharp decrease in water-borne As (Fig. 1e) and all the other elements during the initial 2 h of the experiment (Fig. 1f–o). The water-borne Pb was almost completely removed from the solution (Fig. 1f) and this may be attributed to the formation of highly insoluble lead salts such as $PbSO_4$, $Pb_3(PO_4)_2$ or/and $Pb_3(AsO_4)_2$ The drop in water-borne Ca, Cd, Cu, Mg, Mn and Zn (Fig. 1g, h, i, m, n and o) during the initial 2 h can also be explained by the formation of sparsely soluble or "insoluble" metal phosphates and arsenates [2]. In the case of Ca, formation of sparingly soluble $CaSO_4$ was also likely. However, in comparison with Pb, the amount of each of these metals being immobilized during the initial 2 h only accounted for a smaller proportion of the total amount present in the reacting solution. Since the total Fe in the solution did not show a decrease during the initial 2 h, it was unlikely that either ferrous or ferric phosphates/arsenates precipitated during this period. It is not clear why substantial amount of water-borne K disappeared from the solution (Fig. 1j). Jarosite was unlikely to form during the initial 2 h because no aqueous Fe was removed from the solution during the same period. The only explanation is that K co-precipitated with other metals to form solid solutions [27]. Both water-borne As and P had similar variation pattern over time, showing continuous decrease, with fluctuation, from the 70th to 374th h and then maintained at around 0.36 mmol L^{-1} and 1.0 mmol L^{-1}, respectively (Fig. 1e and l). This trend was more or less consistent with that of the total Fe, suggesting a close association between Fe and these two oxyanion-forming elements except during the initial 116 h of the experiment.

3.2. Chemical composition and identifiable minerals in the precipitates

The major elements in the precipitate collected at the 996th h (at the end of Phase I) was in the following decreasing order: Fe > P > S > As > Pb > K > Mg > Mn > Zn > Cu > Cd, more or less consistent with the order observed for the elements that were removed from the solution at the end of Phase I (Table 1 and Fig. 1). The atomic concentration of precipitate-Fe, -P, -S, -As and -Pb accounted for about 41, 35, 12, 6.8 and 3.9% of the sum of the above 11 elements. The percentage of other elements was <0.6% of the sum. These results infer the dominant presence of iron, phosphate and arsenate species. However, both XRD and RS analyses did not reveal any individual iron phosphate and arsenate mineral phases. Anglesite ($PbSO_4$) was the only identifiable mineral phase in the precipitate by these methods (Fig. 2). This suggests the formation of a mixed iron phosphate and arsenate solid solution, which could not be detected by the XRD and RS techniques. The strong characteristic XRD and RS peaks of anglesite indicate that the solution Pb was predominantly bound to sulfate rather than phosphate and arsenate. This may be attributed to the much higher concentration of sulfate (56 mmol L^{-1}), relative to either phosphate (2.7 mmol L^{-1}) or arsenate (0.8 mmol L^{-1}) in the acid sulfate water. The molar ratio of S to Pb in the precipitate was over 1.7. This implies that about 41% of the precipitate-SO_4 was either structurally or surfacially bound to the iron compounds. Based on the chemical composition, it was unlikely that schwertmannite, if any, was present in a significant amount in the precipitate. The

Table 1
Chemical composition (mmol/kg) of the precipitates collected at the 996th and 3460th h of the incubation experiment.

Element	996th h	3460th h
As	604	611
Cd	0.21	0.20
Cu	1.70	1.56
Fe	3635	3585
K	53.7	49.6
Mg	4.11	4.16
Mn	1.73	1.58
P	3086	3060
Pb	342	281
S	1095	1090
Zn	1.71	1.46

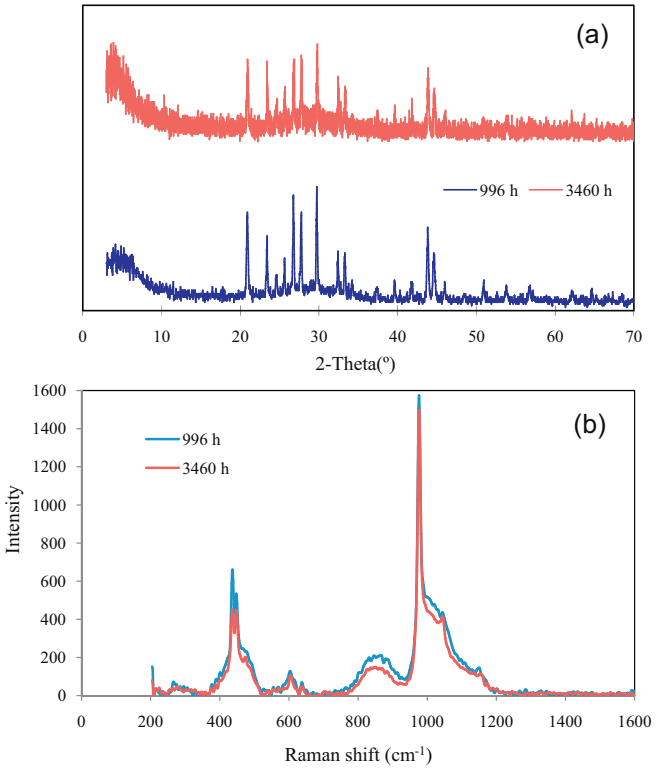

Fig. 2. A comparison between (a) powder X-ray diffractograms and (b) Raman spectra of the ochreous precipitates collected at the 996th h and the 3460th h of the incubation experiment.

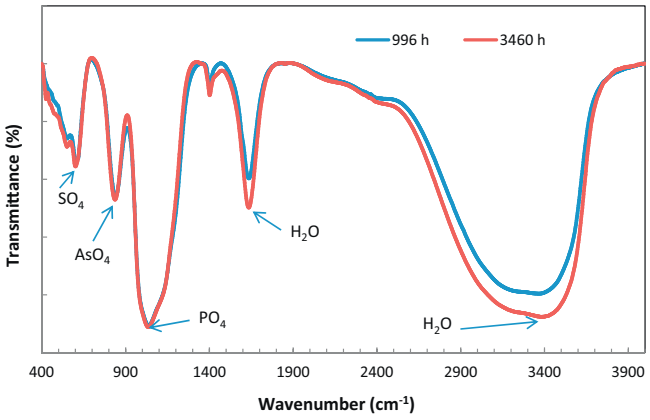

Fig. 3. FTIR spectra of the ochreous precipitates collected at the 996th h and the 3460th h of the incubation experiment.

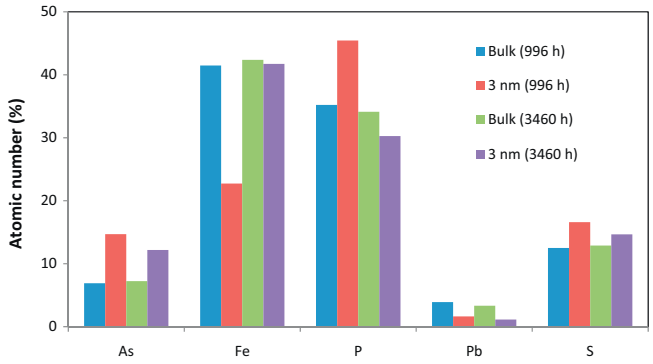

Fig. 4. A comparison of the major chemical constituents between the bulk precipitated material and the ~3 nm-thick outermost surface layer of the precipitate particle.

SEM image of the precipitate shows no characteristic sea-urchin morphology of schwertmannite (Fig. S1a in Supplementary Information). This is in contrast with the predominant presence of schwertmannite precipitated from the modified 9 K solution only system (Fig. S1b and Fig. S2 in Supplementary Information).

FTIR spectrum of the precipitate shows the presence of absorption bands at 3400 cm^{-1}, 1636 cm^{-1}, 1036 cm^{-1}, 819 cm^{-1} and 590 cm^{-1} (Fig. 3). The absorption bands at 3400 cm^{-1} and 1636 cm^{-1} are characteristic of hydroxyl groups from molecules [28]. Phosphate could resulted in absorption bands in the region between 1000 and 1100 cm^{-1} [28–30]. The absorption band at 590 cm^{-1} may be attributed to sulfate [31] and the absorption band at 819 cm^{-1} can be assigned to arenate [32]. Since the molar ratio of cationic Fe (Fe^{3+}) to the sum of oxyanion-forming P and As (PO_4^{3-} and AsO_4^{3-}) was less than 1, it was highly unlikely that any hydroxyl group was incorporated into the mineral structure. Therefore the absorption bands at 3400 cm^{-1} and 1636 cm^{-1} should be attributed to hydroxyl group from water molecules. On the other hand, some hydrogen phosphate or hydrogen arsenate species must have been present in the precipitate to allow valence balance.

The concentration of the major elements contained in the precipitate collected at the 3460th h was very similar to that collected at the 996th h except that Pb concentration was over 15% less in the former than in the latter (Table 1). This indicates that no marked change in chemical composition of the precipitate during the aging period from the 996th to the 3460th h. The reduced proportion of Pb can be attributed to the dilution effect by the new precipitated materials formed after Phase I. Since almost all of the Pb was removed from the solution during Phase I, no more anglesite was formed during Phase II of the experiment.

There was no marked difference in the X-ray diffractogram and RS spectrum between the precipitate collected at the 996th h and that collected at the 3460th h (Fig. 2). FTIR spectra of the precipitates collected at the 996th h and the 3460th h also had a high degree of similarity (Fig. 3). These results indicate that the 2464 h-long aging did not result in the formation of new identifiable mineral phases, suggesting that the crystallization of the mixed iron, arsenate, phosphate, and possibly sulfate solid solution was kinetically slow.

3.3. Comparison between surface and bulk chemical composition of the precipitates

Fig. 4 gives a comparison of the major chemical constituents between the bulk precipitated material and the ~3 nm-thick outermost surface layer (as indicated by XPS results). It can be seen that at the 996th h, the atomic concentration of all oxyanion-forming elements (As, P and S) was lower in the bulk precipitated material than in the outermost layer while the opposite trend was observed for the cationic metals (Fe and Pb). The increased proportion of oxyanion-forming elements on the precipitate surface suggests that the surface-bound arsenate, phosphate and sulfate species tended to be in higher-valent forms to allow more As, P and S being adsorbed to per unit of surface Fe-derived binding site. The dominant arsenate, phosphate and sulfate ion species at a pH around 2 are arsenic acid ($H_3AsO_4^0$), dihydrogen arsenates ($H_2AsO_4^-$), phosphoric acid ($H_3PO_4^0$), dihydrogen phosphates ($H_2PO_4^-$), and hydrogen sulfate (HSO_4^-) as predicted by thermodynamic calculation [33]. As a result of relative enrichment of oxyanionic elements, the relative proportion of iron in the outermost surface layer was reduced, as compared to the bulk. The molar ratio of the surface-As to the bulk-As (2.16) in the precipitate was much greater than that for P (1.29) and S (1.33), indicating an increased capacity of As to compete with P and S for available binding sites from the co-precipitation stage to the subsequent surface complexation/adsorption stage.

It is interesting to note that after aging for another 2464 h, the relative proportion of surface-P markedly decreased while the relative proportion of surface-Fe increased accordingly. Slight decrease in the relative proportion of surface-As and -S was also observed. This indicates that aging caused release of the adsorbed anions from the precipitate with the adsorbed phosphate species being the one that was most susceptible to desorption.

3.4. Chemical states of elements on the surfaces of precipitate particle

The curve-fitted narrow scan XPS spectra of Fe 2p, S 2p, O 1s, As 3d, Pb 4f and P 2p for the particle surfaces had a high similarity between the precipitate collected at the 996th h and that collected at the 3460th h (Fig. 5). The Fe $2p_{3/2}$ spectra had two major peaks centred at 711.4 eV and 713.1 eV, respectively (Fig. 5a and Table 2), which can be assigned to Fe^{3+} bonded to O^{2-} [34–36] as part of the surface-bound arsenate, phosphate and sulfate species. This suggests that aqueous ferrous ion was not involved in surface-binding process. The S 2p peak positions occurred in the region ranging from 168.5 to 170.5 eV, which is characteristic of sulfate-S. This was consistent with the known presence of surface-bound sulfate species. The O 1s peaks centred at 530.9 eV and 531.6 eV for the precipitate collected at the 996th h and 531.3 eV for the precipitate collected at the 3460th h can be attributed to O^{2-} bonded to iron, arsenate, phosphate and sulfate species while the peaks at the higher binding energy side can be assigned to oxygen as part of the adsorbed water molecules. The shift of XPS As 3d peak position to the higher binding

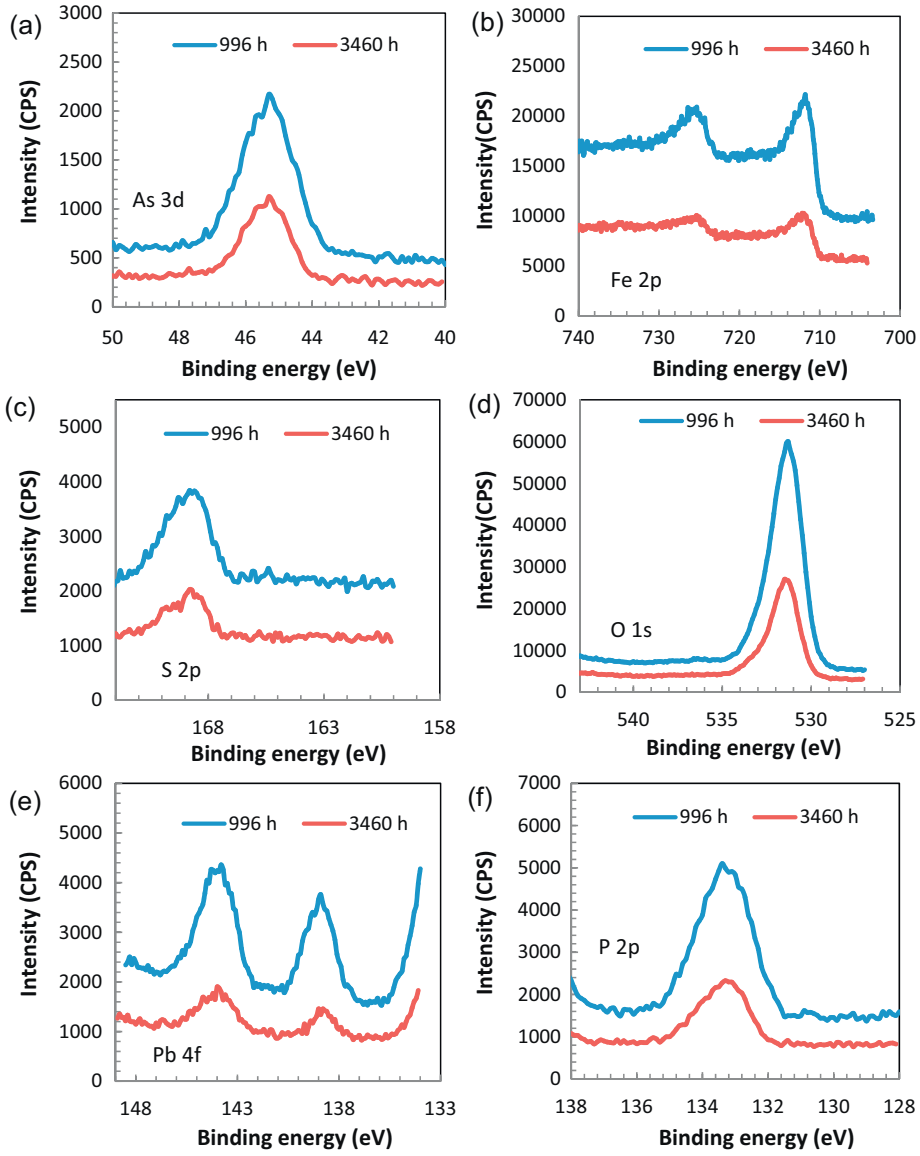

Fig. 5. The curve-fitted narrow scan XPS spectra of (a) Fe 2p, (b) S 2p, (c) O 1s, (d) As 3d, (e) Pb 4f, and (f) P 2p for the particle surfaces of the precipitates collected at the 996th h and the 3460th h of the incubation experiment.

energy side reflects the result of protonation of arsenate species [37]. The precipitate collected at the 996th h had two peaks centred at 45.01 eV and 45.83 eV, which can be assigned to AsO_4^{3-} and $HAsO_4^{2-}/H_2AsO_4^{-}$, respectively. After aging for another 2464 h, there was a major change in the XPS As 3d component, showing a single peak centred at 45.32 eV, which is attributable to $HAsO_4^{2-}$. This appears to suggest that the surface of newly formed precipitate particles tended to accommodate a diverse range of arsenate species with different degree of protonation. Aging led to the rearrangement of surface chemical states with $HAsO_4^{2-}$ being the dominant adsorbed arsenate species. The XPS Pb 4f spectrum of the precipitate collected at the 996th h consisted of two doublet peaks: 138.8 eV (143.3 eV) and 139.7 eV (144.1 eV), which fell within the range of sulfite- to sulfate-bound Pb [38,39]. Since the S 2p signal showed no peak corresponding to sulfite-S, the presence of sulfite-Pb can be excluded. The XPS P 2p spectra from both precipitate samples collected at the 996th h and the 3460th h revealed a single peak centred at 133.3 eV, indicating that HPO_4^{2-} was the dominant species adsorbed on the surface of the precipitate particles [40].

3.5. Arsenate immobilization mechanisms

At the initial stage (within 2 h of the experiment) before sufficient amount of ferric ion was produced from microbial oxidation of ferrous ion, arsenate species tended to reacted with the non-Fe metals (except for Pb) to form sparsely soluble mixed metals, arsenate, phosphate and sulfate compounds. It is likely that these mixed compounds were poorly crystalline and possibly in the forms of solid solution, as inferred by the XRD results showing the absence of any individual arsenate and phosphate minerals.

Subsequently when sufficient amount of ferric ion was generated, ferric ion played a dominant role in binding the arsenate species. This can be described by the following generic chemical equations:

$$a\mathrm{Fe}^{3+} + b\mathrm{H_3AsO_4} + (a-b)\mathrm{H_3PO_4} \rightarrow \mathrm{Fe}_a(\mathrm{AsO_4})_b(\mathrm{PO_4})_{(a-b)} + (a\times 3)\mathrm{H}^{+} \quad (1)$$

Table 2
Binding energy and atomic concentration of the major peaks in the Fe 2p3/2, S 2p, O 1s, As 3d, Pb 4f and P 2p XPS spectra.

	Binding energy (eV)	Atomic (%)
Fe 2p3/2		
996 h	711.4	72.1
	713.1	27.9
3460 h	713.13	52.1
	711.59	47.9
S 2p		
996 h	168.46	52.3
	169.51	28.6
	170.49	19.2
3460 h	168.55	67.3
	169.78	32.7
O 1s		
996 h	530.9	23.5
	531.6	67.5
	533.0	9.00
3460 h	531.3	71.6
	532.5	28.4
As 3d		
996 h	45.01	53
	45.83	47
3460 h	45.32	100
Pb 4f		
996 h	138.8	36.1
	139.7	5.1
	143.3	6.9
	144.1	52
3460 h	138.7	36.9
	139.6	5.2
	143.3	6.3
	144.2	
P 2p		
996 h	133.3	100
3460 h	133.3	100

$$a\mathrm{Fe}^{3+} + b\mathrm{H_2AsO_4}^{-} + (a-b)\mathrm{H_2PO_4}^{-} \rightarrow \mathrm{Fe}_a(\mathrm{AsO_4})_b(\mathrm{PO_4})_{(a-b)} + (a\times 2)\mathrm{H}^{+} \quad (2)$$

$$a\mathrm{Fe}^{3+} + b\mathrm{HAsO_4}^{2-} + (a-b)\mathrm{HPO_4}^{2-} \rightarrow \mathrm{Fe}_a(\mathrm{AsO_4})_b(\mathrm{PO_4})_{(a-b)} + (a\times 1)\mathrm{H}^{+} \quad (3)$$

At a solution pH around 2, arsenic acid (H_3AsO_4), dihydrogen arsenate ($H_2AsO_4^-$), phosphoric acid (H_3PO_4) and dihydrogen phosphate ($H_2PO_4^-$) dominated the arsenate and phosphate species [30]. Therefore, Eqs. (1) and (2) type of reactions was the logical pathways leading to the formation of a mixed iron, arsenate and phosphate mineral phase, which was likely to be poorly crystalline. Small amounts of sulfate might be incorporated into the solid solution. This is supported by the fact that the chemical, RS and FTIR analyses all indicated the presence of arsenate, phosphate and sulfate in the precipitates but the XRD analysis showed the absence of any individual arsenate and phosphate minerals.

The last stage of arsenate immobilization mainly involved surface complexation. The interaction between the aqueous arsenic acid and dihydrogen arsenate with the surface of the precipitate particles resulted in the protonation of the surface-bound arsenate, as expressed by the following chemical equations:

$$[\text{Precipitate-Fe}^{3+}]\text{-AsO}_4^{3-} + \mathrm{H_3AsO_4} \rightarrow \{[\text{Precipitate-Fe}^{3+}]\text{-HAsO}_4^{2-}\}^{+}\text{-H}_2\text{AsO}_4^{-} \quad (4)$$

$$[\text{Precipitate-Fe}^{3+}]\text{-AsO}_4^{3-} + \mathrm{H_3AsO_4} \rightarrow \{[\text{Precipitate-Fe}^{3+}]\text{-H}_2\text{AsO}_4\}^{2+}\text{-HAsO}_4^{2-} \quad (5)$$

The bonding involving $H_2AsO_4^-$ and $HAsO_4^{2-}$ increased the capacity of per unit surface-Fe to carry adsorbed As, as demonstrated in Eqs. (4) and (5). The higher percentage of surface-bound As in the sum of all the detected surface elements (as indicated by XPS results), relative to the percentage of the bulk As in the sum of all the detected elements in the bulk precipitate sample (as indicated by the chemical analysis), supports the above hypothesis.

In abiotic precipitation experiments involving reactions between ferric nitrate, sodium sulfate and sodium hydrogen arsenate at 60 °C, Carlson et al. [11] observed that schwertmannite was replaced as the dominant phase by a poorly crystalline ferric hydroxyl arsenate when mole As/Fe ratios exceeded 0.15. The molar ratio As/Fe of our experiment was 0.08, which is below the above limit. However, no schwertmannite and ferric hydroxyl arsenate were detected in this study. This appears to reflect the apparent difference in the precipitation process between the abiotic experiment and the microbially-mediated experiment. In the former, the initial state of iron was in ferric form, which was readily available for ochre precipitation. However in the latter, the availability of ferric ion was limited for the reaction with arsenate species, resulting in a much higher As/Fe(III) molar ratio in the earlier stage of ochre precipitation. This may partly explain the absence of schwertmannite in this study. On the other hand, the presence of phosphate and various metals could also markedly interfere the ochre precipitation. In natural acid mine drainage scenarios, arsenate immobilization through formation of scorodite ($FeAsO_4{\cdot}2H_2O$) was observed [15]. However, due to the poorly crystalline nature of the mixed metal, arsenate and phosphate solid solution phases, it is difficult to isolate and identify such materials from the streambed sediments affected by acid mine drainage. The results obtained from this study have implications for understanding the arsenate immobilization in acid mine drainage scenarios by demonstrating the presence of such materials in the laboratory simulation system.

4. Conclusion

The experimental results obtained from this study provide the insights into the mechanisms of arsenate immobilization associated with microbial oxidation of ferrous ion in a complex acid sulfate water system at initial pH of 2. The removal of arsenate from the acid sulfate water can be described as a three-stage process through which the aqueous arsenate species were progressively immobilized. Arsenate was initially immobilized through co-precipitation with non-Fe metals and phosphate. Subsequently when sufficient ferric ion was produced from microbial oxidation of ferrous ion, formation of a mixed iron, arsenate and phosphate mineral phase predominated. The last stage of arsenate immobilization involved surface complexation. Pb appeared to play an insignificant role in arsenate immobilization due to its strong affinity for sulfate to form sparsely soluble anglesite. Phosphate strongly competed with arsenate for the available binding sites at all the stage. However, As exhibited an increased capacity to compete with P and S for available binding sites from the co-precipitation stage to the subsequent surface complexation stage. Adsorbed As tended to be in $HAsO_4^{2-}$ form. There were no marked changes in both bulk As and surface As of the ochreous precipitate after 2464-h aging, suggesting the scavenged arsenate species was relatively stable under the experimental conditions set for this study. The presence of As, Cu, Cd, Pb, Zn and Mn in the acid sulfate water system in this study inhibited the precipitation of schwertmannite. As a consequence, arsenate immobilization observed in this study was not related to the formation of schwertmannite and its derivatives such as goethite and jarosite.

Acknowledgements

This work was financially supported by the Natural Science Foundation of China (Project numbers: 40471067 and 40773058) and the Guangdong Bureau of Science and Technology (Project No. 2005A30402006).

Appendix A. Supplementary data

Supplementary data associated with this article can be found, in the online version, at doi:10.1016/j.jhazmat.2012.03.021.

References

[1] A.G. Gault, D.R. Cooke, A.T. Townsend, J.M. Charnock, D.A Polya, Mechanisms of arsenic attenuation in acid mine drainage from Mount Bischoff, western Tasmania, Sci. Total Environ. 345 (2005) 219–228.
[2] H.F. Cheng, Y. Hu, J. Luo, B. Xu, J.F Zhao, Geochemical processes controlling fate and transport of arsenic in acid mine drainage (AMD) and natural systems, J. Hazard. Mater. 165 (2009) 13–26.
[3] J.M. Bigham, L. Carlson, E. Murad, Schwertmannite, a new iron oxyhydroxysulphate from Pyhasalmi, Finland, and other localities, Mineral. Mag. 58 (1994) 641–648.
[4] J.M. Bigham, U. Schwertmann, S.J. Traina, R.L. Winland, M. Wolf, Schwertmannite and the chemical modeling of iron in acid sulfate waters, Geochim. Cosmochim. Acta 60 (1996) 2111–2121.
[5] S. Regenspurg, A. Brand, S. Peiffer, Formation and stability of schwertmannite in acidic mining lakes, Geochim. Cosmochim. Acta 68 (2004) 1185–1197.
[6] J. Jonsson, P. Persson, S. Sjoberg, L. Lovgren, Schwertmannite precipitated from acid mine drainage: phase transformation, sulphate release and surface properties, Appl. Geochem. 20 (2005) 179–191.
[7] A.W. Schroth, R.A. Parnell Jr., Trace metal retention through the schwertmannite to goethite transformation as observed in a field setting, Alta Mine, MT, Appl. Geochem. 20 (2005) 907–917.
[8] P. Acero, C. Ayora, C. Torrentó, J.M. Nieto, The role of trace elements during schwertmannite precipitation and subsequent transformation into goethite and jarosite, Geochim. Cosmochim. Acta 70 (2006) 4130–4139.
[9] H.M. Wang, J.M. Bigham, O.H. Tuovinen, Formation of schwertmannite and its transformation to jarosite in the presence of acidophilic iron-oxidizing microorganisms, in: Second Asian Symposium on Biomineralization (ASB-2), Mater Sci. Eng. C 26 (2006) 588–592.
[10] Y.H. Liao, L.X. Zhou, J.R. Liang, H.X. Xiong, Biosynthesis of schwertmannite by *Acidithiobacillus ferrooxidans* cell suspensions under different pH condition, Mater. Sci. Eng. C 29 (2009) 211–215.
[11] L. Carlson, J.M. Bigham, U. Schwertmann, A. Kyek, A. Qagner, Scavenging of As from acid mine drainage by schwertmannite and ferrihydrite: a comparison with synthetic analogues, Environ. Sci. Technol. 36 (2002) 1712–1719.
[12] A. Courtin-Nomade, H. Bril, C. Neel, J.F. Lenain, Arsenic in iron cements developed within tailings of a former metalliferous mine, Enguiales, Aveyron, France, Appl. Geochem. 18 (2003) 395–408.
[13] M.P. Asta, J. Cama, M. Martínez, J. Giménez, Arsenic removal by goethite and jarosite in acidic conditions and its environmental implications, J. Hazard. Mater. 171 (2009) 965–972.
[14] K. Fukushi, M. Sasaki, T. Sato, N. Yanase, H. Amano, H. Ikeda, A natural attenuation of arsenic in drainage from an abandoned arsenic mine dump, Appl. Geochem. 18 (2003) 1267–1278.
[15] L. Haffert, D. Craw, Processes of attenuation of dissolved arsenic downstream from historic gold mine sites, New Zealand, Sci. Total Environ. 405 (2008) 286–300.
[16] M.P. Asta, C. Ayora, P. Acero, J. Cama, Field rates for natural attenuation of arsenic in Tinto Santa Rosa acid mine drainage (SW Spain), J. Hazard. Mater. 177 (2001) 1102–1111.
[17] K. Fukushi, T. Sato, N. Yanase, J. Minato, H. Yamada, Arsenate sorption on schwertmannite, Am. Mineral. 89 (2004) 1728–1734.
[18] E.D. Burton, R.T. Bush, S.G. Johnston, K.M. Watling, R.K. Hocking, L.A. Sullivan, G.K. Parker, Sorption of Arsenic(V) and Arsenic(III) to Schwertmannite, Environ. Sci. Technol. 43 (2009) 9202–9207.
[19] S. Regenspurg, S. Peiffer, Arsenate and chromate incorporation in schwertmannite, Appl. Geochem. 20 (2005) 1226–1239.
[20] P.C. Singer, W. Stumm, Acid mine drainage: the rate-determining step, Science 167 (1970) 1121–1123.
[21] G.J. Olson, Rate of pyrite bioleaching by *Thiobacillus ferrooxidans*: results of an interlaboratory comparison, Appl. Environ. Microbiol. 57 (1991) 642–644.
[22] K. Benzerara, G. Morin, T.H. Yoon, J. Miot, T. Tyliszczak, C. Casiot, O. Bruneel, F. Farges, G.E. Brown Jr., Nanoscale study of As biomineralization in an acid mine drainage system, Geochim. Cosmochim. Acta 72 (2008) 3949–3963.
[23] C.S. Chan, S.C. Fakra, D.C. Edwards, D. Emerson, J.F. Banfield, Iron oxyhydroxide mineralization on microbial extracellular polysaccharides, Geochim. Cosmochim. Acta 73 (2009) 3807–3818.
[24] J. Zhou, Y. Niu, W. Qin, Effects of sulfide minerals on *Acidithiobacillus ferrooxidans*, Chin. J. Nonferrous Met. 13 (2003) 1278–1282.
[25] R.H. Byrne, Y.R. Luo, R.W. Young, Iron hydrolysis and solubility revisited: observations and comments on iron hydrolysis characterizations, Mar. Chem. 70 (2000) 23–35.
[26] B.G. Lottermoser, Mine Wastes: Characterization, Treatment and Environmental Impacts, 3rd ed., Springer-Verlag, Berlin, Heidelberg, 2010, 400 pp.
[27] J. Kushnir, The coprecipitation of strontium, magnesium, sodium, potassium and chloride ions with gypsum. An experimental study, Geochim. Cosmochim. Acta 44 (1980) 1471–1482.
[28] P. Bonnet, J.M.M. Millet, C. Leclercq, J.C. Védrine, Study of a new iron phosphate catalyst for oxidative dehydrogenation of isobutyric acid, J. Catal. 158 (1965) 128–141.
[29] Y. Arai1, D.L. Sparks, ATR–FTIR spectroscopic investigation on phosphate adsorption mechanisms at the ferrihydrite–water interface, J. Colloid Interface Sci. 241 (2001) 317–326.
[30] D. Yu, C. Wu, Y. Kong, N. Xue, X. Guo, W. Ding, Structural and catalytic investigation of mesoporous iron phosphate, J. Phys. Chem. C 111 (2007) 14394–14399.
[31] J.F. Boily, P.L. Gassman, T. Peretyazhko, J. Szanyi, J.M. Zachara, FTIR spectral components of schwertmannite, Environ. Sci. Technol. 44 (2010) 1185–1190.
[32] S.L. Wang, C.N. Mulligan, Speciation and surface structure of inorganic arsenic in solid phases: a review, Environ. Int. 34 (2008) 867–879.
[33] National Institute of Advanced Industrial Science Technology, Atlas of Eh-pH Diagrams – Intercomparison of thermodynamic databases, in: Geological Survey of Japan Open File Report, Naoto, Takeno, 2005.
[34] H.W. Nesbitt, G.M. Bancroft, A.R. Pratt, M.J. Scaini, Sulfur and iron surface states on fractured pyrite surfaces, Am. Mineral. 83 (1998) 1067–1076.
[35] W. Han, M.Y. Gao, Investigations on iron sulfide nanosheets prepared via a single-source precursor approach, Cryst. Growth Des. 8 (2008) 1023–1030.
[36] Y. Cai, Y. Pan, J. Xue, Q. Sun, G. Su, X. Li, Comparative XPS study between experimentally and naturally weathered pyrites, Appl. Surf. Sci. 255 (2009) 8750–8760.
[37] S. Zhang, X. Li, J.P. Chen, An XPS study for mechanisms of arsenate adsorption onto a magnetite-doped activated carbon fiber, J. Colloid Interface Sci. 343 (2010) 232–238.
[38] B.J. James, R. Cameron, C. Baskcomb, Selected area XPS analysis for identification of pigment compounds in microscopic paint flakes, Res. Lett. Mater. Sci. (2008) 1–4.
[39] G. Konstantatos, L. Levina, A. Fischer, E.H. Sargent, Engineering the temporal response of photoconductive photodetectors via selective introduction of surface trap states, Nano Lett. 8 (2008) 1446–1450.
[40] R.K. Vempati, R.H. Loeppert, D.L. Cocke, Mineralogy and reactivity of amorphous Si-ferrihydrites, Solid State Ionics 38 (1990) 53–61.